ACS AGRICULTURAL SCIENCE & TECHNOLOGY

Open Access

pubs.acs.org/acsagscitech

Article

Detection of Airborne Pathogenic Wheat Rust Spores Using Machine-Learning-Assisted Optical Imaging

Sebastian Kalt,* Berthold Wegner, Max Strauß, Lenon Romano Modesto, Tim Alletzhäusser, Philipp Schulz, Tzenka Miteva, and Martin Wegener*

Cite This: *ACS Agric. Sci. Technol.* 2026, 6, 586−598

Read Online

ACCESS | Metrics & More | Article Recommendations | Supporting Information

ABSTRACT: Fast localization and monitoring of airborne pathogens, such as fungal spores, are crucial for efficient crop disease management. Wheat rust fungi represent a major threat, as their urediniospores disperse rapidly via wind or raindrops, causing severe crop damage and yield losses. Given that wheat is the most extensively cultivated crop worldwide, outbreaks of rust diseases pose a significant risk to global food security. In this work, we present a compact optical imaging platform integrated with a machine-learning-based classification algorithm, forming an autonomous sentinel unit for in-field detection and identification of airborne urediniospores of wheat rusts. This automated device collects multichannel images of airborne particles under different illumination conditions, including a luminescence channel, and processes them using a Bayesian algorithm for fast image segmentation and spore identification within minutes and achieves an F_1 score of 97.7% for spore detection and 91.6% for identifying wheat rust spores. Using this system, wheat rust diseases can be localized in their early development stages, and preventative control strategies deployed even before the first symptoms become visible.

KEYWORDS: *biosensing, machine learning, fungal spores, wheat rust, Puccinia striiformis f.sp. tritici, Puccinia triticina, airborne pathogens, disease monitoring, spore tracking*

1. INTRODUCTION

Airborne pathogens are not only a highly discussed topic in the human health sector but also highly relevant in the context of botany, agriculture, and food production. Plant pathogens such as fungal spores can rapidly spread as they are carried by wind, animals including humans, or man-made machines over long distances.[1−5] As a consequence, these pathogens can cause severe damage to crop plants, leading to significant yield losses.[6−8] If the environmental conditions such as weather and host availability are suitable, the corresponding diseases can reach the level of epidemics or even pandemics threatening the local and global food production.[9−12]

As wheat covers more area than every other food crop and is also the third most produced crop in the world,[13] wheat plants are at a constant threat by a large variety of pests and ever-evolving pathogens with a significant potential for serious economic damage, rising food prices, or even food shortages. As a consequence, wheat losses are estimated to be about 21.5% per year on the global average but can even reach up to 28.1% in Mainland China or 24.9% in Northwestern Europe on the annual average.[14]

Wheat leaf rust (wheat brown rust, *Puccinia triticina*, *Pt*) and wheat stripe rust (wheat yellow rust, *Puccinia striiformis* f.sp. *tritici*, *Pst*) are biotrophic fungi that are specialized in infecting wheat by airborne urediniospores.[15,16] Due to the rapid asexual reproduction of a large number of urediniospores, both fungi combined are responsible for approximately 24.8% of all wheat losses in the global annual average and even for 33.4% in Northwestern Europe.[14]

Hence, researchers all over the world are searching for strategies to fight the spread of rust fungi and fungal crop diseases in general. The most pursued approaches include, among others, the analysis of old and the search for new genetic races to make the host plants resistant or at least less susceptible to fungal infections[17−24] as well as the development of more potent fungicides.[25−27] Other strategies rely on persistent disease and symptom monitoring or spore tracking to predict[28] and contain the spreading of crop diseases by identifying and destroying the infected plants and a preventative spraying using suitable fungicides.[29]

As artificial intelligence, particularly machine-learning methods, grows in popularity every day, many disease-monitoring approaches utilize optical imaging,[30−32] light diffraction,[33] or spectral data[34−36] in combination with machine-learning tools. In this context, spores are often collected with conventional spore traps and pictures are subsequently taken in a laboratory environment and analyzed manually or with automated image segmentation tools.[37,38] Alternatively, molecular sample-analysis methods such as targeting DNA for identification are used.[39,40] In all of these cases, some collection time and manual sample transfer are required.

Received: September 18, 2025
Revised: February 7, 2026
Accepted: February 10, 2026
Published: March 14, 2026

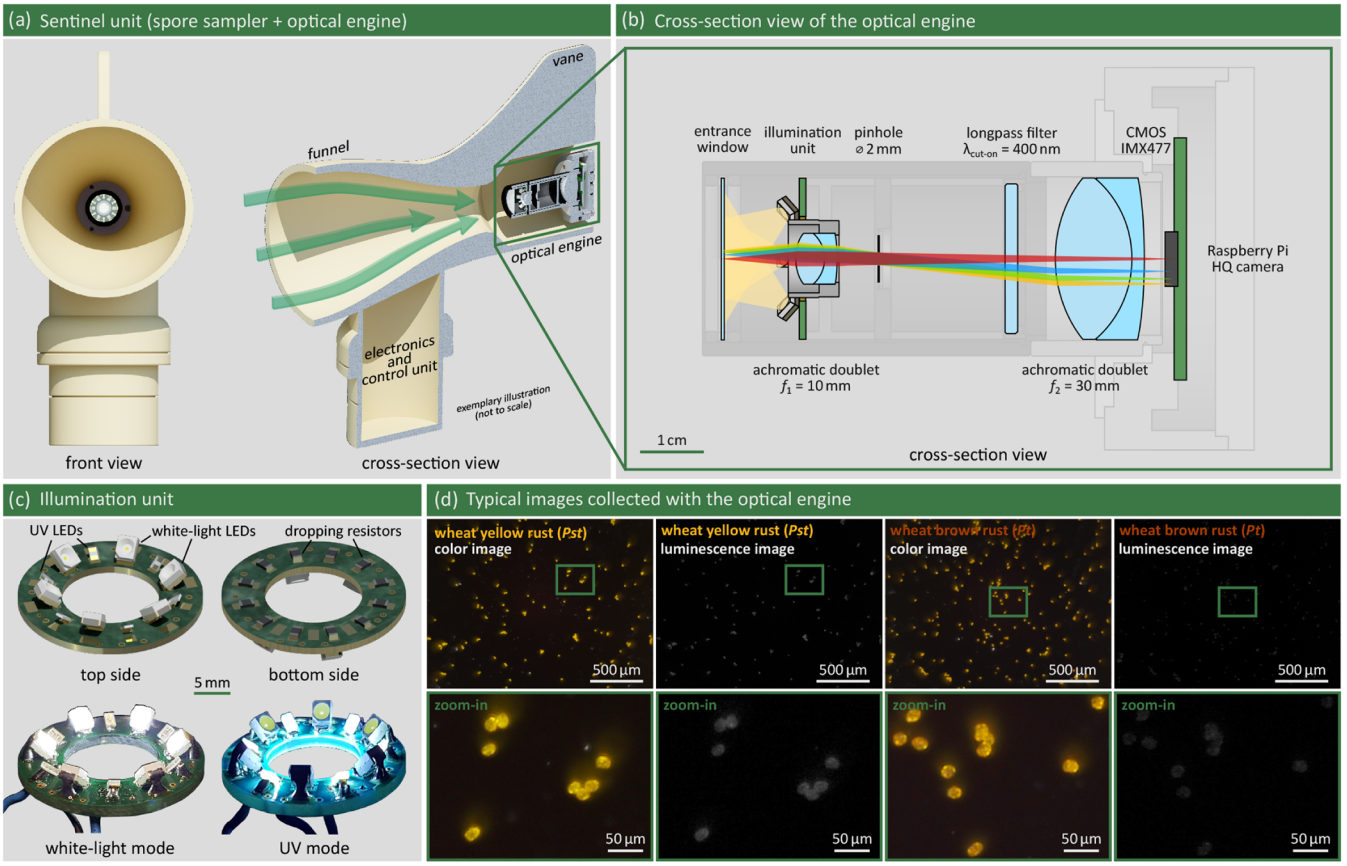

Figure 1. Overview of the sentinel unit used to detect wheat yellow rust and wheat brown rust spores. (a) Passive spore sampler and optical engine. (b) Cross-sectional view of the optical engine. The airborne particles land on the collagen-coated entrance window on the left-hand side. The entrance window, which is mounted with other coated glass substrates on a wheel (not shown), is imaged onto an IMX477 CMOS sensor as part of a Raspberry Pi HQ camera by an achromatic and telecentric imaging system using a 2.85× magnification. (c) Rendered detail views and captured pictures of the illumination unit, a ring-shaped printed circuit board with two independent circuits connecting six white-light-emitting surface-mounted LEDs and six near-ultraviolet surface-mounted LEDs, respectively. (d) Typical images of wheat yellow and brown rust urediniospores collected with the presented imaging unit under the two illumination conditions.

Alternative approaches focus on taking macroscopic images of the wheat plants or their leaves from unmanned aerial vehicles[41,42] (UAVs), satellites,[43−45] with specialized sensing units, or even with smartphone cameras.[46] These methods, however, mainly rely on observable symptoms such as visible uredinia or chlorosis developed by the wheat plant.[47,48] For wheat stripe rust, the first visible symptoms start with chlorosis about 7 days after inoculation, but uredinia do not become apparent earlier than 12 to 14 days after inoculation under ideal conditions.[49] Hence, there is time lost for all of these approaches that could already be used for countermeasures. Nonetheless, these tools can still be very effective for systematic documentation and assessment of the severity of already spread diseases.

We mention two particularly interesting approaches in the context of this work explicitly. One focuses on a biochemical multilayer sensor mimicking the surface and volatiles of wheat leaves,[50,51] which could be included in an imaging system and therefore in a spore-sensing device. The other one is the commercial sensor PollenSense, an optical imaging device that also uses machine learning for automated image analysis.[52] It has a broad range of applications, including individual consumer needs, but as a result it is not optimized for the specific application discussed here, which needs to detect and identify wheat rust spores with critically high accuracy.

In this work, we present a compact optical imaging unit and machine-learning-based software routine that, together with a passive spore sampler,[51] combines both the collection, detection, and identification of microscopic spores, which are ellipsoidal objects with half-axes between approximately 10 and 13 μm in this case, into one device. Therefore, our device, which we call a "spore sentinel unit", acts as an automated early warning tool for airborne wheat rust spores. It is designed to be operated in agricultural fields as a single device or in a network of sentinel units. Spores and other particles carried by wind are guided by a funnel-shaped spore sampler onto movable and exchangeable glass windows coated with collagen.

The optical engine, which is the centerpiece of this sentinel unit, is a compact achromatic and telecentric imaging system. It is used to take pictures of the collected particles under different lighting conditions such as dark-field white-light and dark-field near-ultraviolet illumination. This allows for supplementing the list of characteristic color-related and geometric features of spores with luminescence properties. These can be used to detect and identify urediniospores of wheat rust fungi in the collected images with a trained Bayesian classification model. Even though the underlying model is trained to identify wheat rust spores in the presented case, it can also be retrained for additional target spore species.

https://doi.org/10.1021/acsagscitech.5c00836
ACS Agric. Sci. Technol. 2026, 6, 586−598

2. MATERIALS AND METHODS

In the following, we present additional details regarding the components of the sentinel unit and the developed software tool for segmenting and analyzing the collected spore images.

2.1. Sentinel Unit

The sentinel unit consists of four main components: An optical engine, a passive spore sampler, a control unit, and a power supply unit, as shown in Figure 1a. It passively collects the airborne spores, takes pictures under different illumination conditions, and transmits the pictures and additional information such as weather data to a computing device for further processing and analysis. This paper focuses on the optical engine as a crucial need for pathogen detection.

The spore sampler, as already published by Blackall et al.,[51] was designed using computational fluid dynamics and Lagrangian particle tracking to act as a so-called air multiplier. This means that the shape of the sampler is optimized to effectively increase the particle density in the sensing area rather than modulating the airflow along the device.[51] Additional information about the spore collection can be found in this publication. As the whole device is mounted on a pivotable socket and equipped with vanes, the spore sampler not only serves to guide the airborne particles onto the sensing area but also passively aligns the device to the wind direction. The spore sampler is 3D printed and houses the control unit and additional electronics.[51]

The optical engine of the presented sentinel unit is illustrated in Figure 1b. It combines all components that are required to collect and transfer spore images to the control unit, i.e., everything from the first optical interface to the printed circuit board used for the image-sensor readout. The spores and other airborne particles are guided by the spore sampler onto a glass window. This window is coated with a thin collagen film to improve the adhesion of the spores and to reduce the formation of multilayer spore clusters.[53] To produce this coating, we used collagen type I with a concentration of 0.01% (w/v). As the spore sampler is designed so that the collagen film is not directly exposed to rain or high-intensity UV light, the film is stable over 8 to 12 weeks, i.e., approximately one spore season. This was confirmed in laboratory experiments where collagen films of this type were exposed to daylight and dew-like conditions within the mentioned time frame.

The particles on the thin coating are illuminated by a custom-made ring light, which can be switched between two different illumination modes. The ring light, as shown in Figure 1c, consists of a ring-shaped printed circuit board (PCB) that is equipped with twelve surface-mounted light-emitting diodes (SMD LEDs) connected in parallel in two different circuits and twelve 82 Ω thick-film dropping resistors. As the SMD LEDs are mounted on the ring light around the imaging beam path facing the entrance window, the particles on the collagen film are illuminated in a reflection-based dark-field configuration. To increase the intensity in the center of the entrance window, the SMD LEDs are mounted at an angle of 40° with respect to the PCB directly aiming at the intersection point of the optical axis and the entrance window. Six SMD LEDs emit bright white light (TRU components, 3528-1573667, PLCC-2 packaging) and are used to collect color images of the particles on the entrance window. The remaining six SMD LEDs are connected in a separate circuit and emit ultraviolet light with a bandwidth of about 10 nm around the center wavelength of 365 nm (Kingbright, KTS-2012UV365). The second illumination mode is used to collect luminescence images to supplement the object-dependent color information extracted from the white-light images with the luminescence data. To reduce the background brightness in both illumination modes due to transmitted light from external light sources, such as the sun, an electrically controlled shutter can be placed in front of the entrance window.

To image the illuminated particles, two doublet lenses and a CMOS sensor are combined to create a simple achromatic and telecentric imaging system as shown in Figure 1b. As white-light illumination and imaging are used, it is important that the system is sufficiently achromatic. In addition, the system is designed to be bitelecentric to reduce parallax error so that the size of the particles can also be used as a characteristic feature for classification.

The imaging system is designed and characterized using ray-tracing tools within Ansys Zemax OpticStudio and optimized to be used with a Sony IMX477 back-illuminated CMOS sensor or a similar device. This sensor was selected because of its compact size while still having a large number of active pixels (4056 × 3040) due to its small pixel size of 1.55 μm. In the context of this work, the IMX477 is used as a mounted version on a Raspberry Pi HQ camera board. The field of view of the imaging system directly translates to the effective sensing area on the entrance window if no stitching methods with multiple fields of view are used. Either way, a large field of view is desirable. In contrast, a large magnification, which corresponds to a high resolution in this simple case, is also advantageous, as more pixels per particle result in a higher information density to be used for object identification. Therefore, we had to find a reasonable compromise between a large field of view and high magnification. As shown in Figures S1 and S2 in the Supporting Information as well as explained in further detail in Supplementary Note 1, we have chosen a design magnification of about 2.85× resulting in a field of view with a diameter of 2.761 mm, which is clipped to approximately 2.207 mm × 1.655 mm by the CMOS sensor. To achieve this magnification, the first achromatic lens (Thorlabs, AC080-010-A-ML) is selected to have a focal length of 10 mm while the tube lens (Thorlabs, AC254-030-A-ML) has a focal length of 30 mm. To keep the system compact, the doublets are placed facing the same direction, which results in a shorter total track length of the imaging system, as the image sensor can be placed closer to the tube lens. Hence, the lenses are not mounted in a conventional 4*f*-configuration but a slightly more compact arrangement. To clean up the beam path and to get a better contrast, a pinhole (Thorlabs, P2000K) with an opening diameter of 2 mm is placed in the Fourier plane. In addition, a long-pass filter (Thorlabs, FELH0400) with a cut-on wavelength of 400 nm is placed into the beam path to remove scattered ultraviolet excitation light. A full list of all components and additional details can be found in Table S1 in the Supporting Information. As the imaging system is intentionally designed to be both compact and cost-effective, small optical deficiencies, such as spherical and comatic aberrations, are accepted here. However, they have to be considered when processing the captured images, as will be discussed in further detail below. The influence of these uncorrected aberrations on the imaging quality can particularly be seen in Figure S1 in the Supporting Information.

The optical engine is operated by a Raspberry Pi Zero 2 W and is interconnected to a low-power wide area (LPWA) wireless communication board based on the Sony ELTRES platform.[51] In principle, image processing and spore identification can also be done on the Raspberry Pi itself if the software code is further optimized to deal with the limited hardware. However, as decreasing the processing time also reduces the sampling time, the images are not processed on the Raspberry Pi in the context of this work but are transmitted wirelessly to a central computation unit. In addition, this central computation unit can also be used to interconnect and communicate wirelessly with multiple sentinel units at the same time, which can then be used to analyze spatial and temporal developments in the occurrence of target spores. Furthermore, the system allows for upgrading the unit by supplementary sensors to collect additional information, such as live weather data.

In the first experiments, the sentinel unit was powered by using a conventional 12 V lead-acid car battery. However, it can in principle also be powered by other mobile power supply options, such as solar cells connected to a battery. The illumination unit, i.e., the SMD LED ring light, is powered by a voltage of 5 V for both illumination modes and is directly controlled by the Raspberry Pi.

Figure 1d exhibits typical examples of images collected by means of the optical engine. This panel contains wide-field optical "color images" and luminescence images from both yellow rust spores and brown rust spores, as well as zoomed-in versions of all of these. With the human eye, one can see slight differences between the two types of spores in the color images. However, the differences in the luminescence images are significantly more pronounced. This means that a distinction between yellow and brown rust spores is likely possible on the basis of either color or luminescence images alone, yet

https://doi.org/10.1021/acsagscitech.5c00836
ACS Agric. Sci. Technol. 2026, 6, 586−598

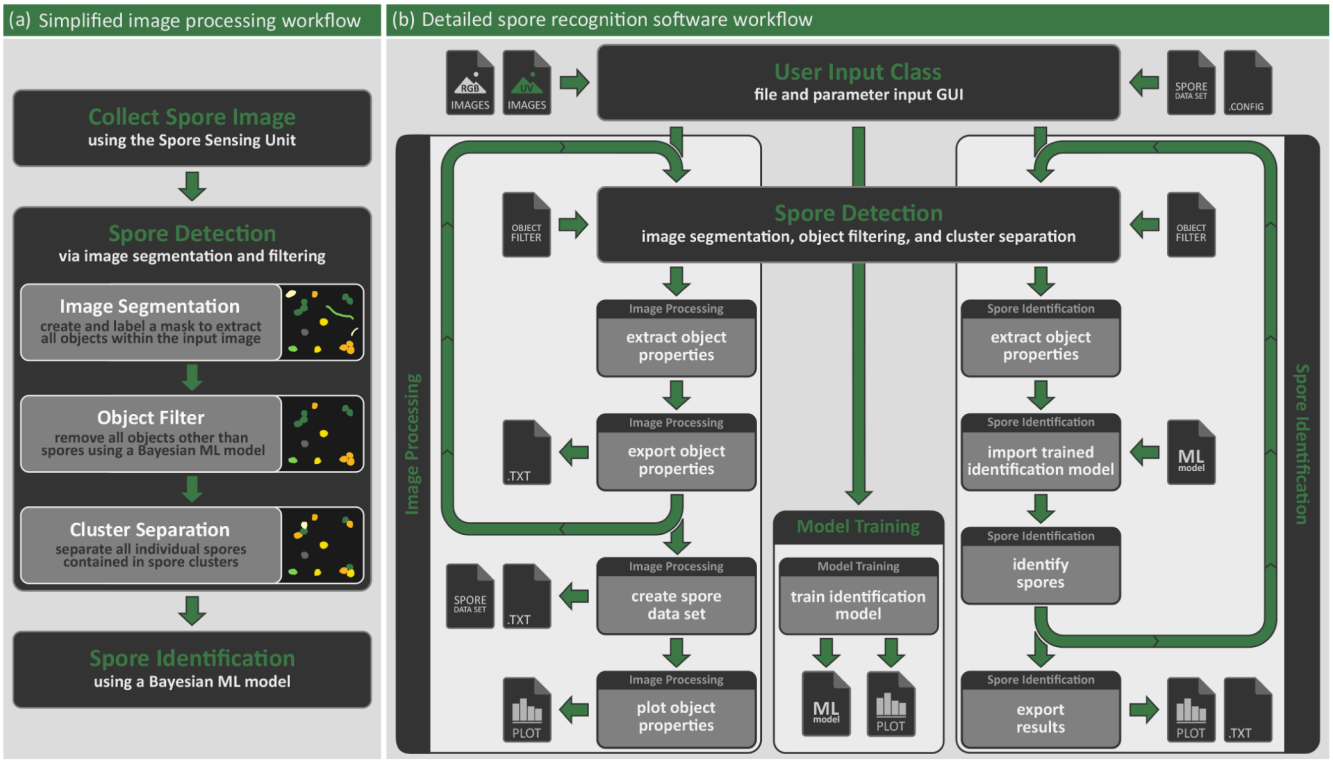

Figure 2. Workflow of the developed spore recognition algorithm. (a) Simplified image-processing workflow. (b) Detailed software workflow including all major classes, function groups, modes of operation, as well as all input and output files.

impeding the classification process by omitting obvious characteristic properties. In our analysis and discussion below, we will include both types of images to obtain optimum classification scores.

2.2. Sample Preparation

To train the identification model, class-labeled samples are required. Therefore, we have prepared small Petri dishes with spores for all laboratory experiments that have the same properties as the entrance window. As mentioned earlier, the entrance windows as well as the mimicking Petri dish bottoms are coated with a thin layer of collagen to improve adhesion and reduce spore clustering. In addition, the Petri dishes used can also be sealed to avoid contamination of the class-labeled samples and to keep the pathogenic spores contained.

Spores from two isolates were used: yellow rust isolate 11/19, a Warrior strain (PstS7), and WB77xR for brown rust. Producing fresh inoculum was made on the wheat cultivar 'Carthago' with 30 seedlings grown together in standard potting soil by Hawita Fruhstorfer Erde treated once with malic acid. Spores were taken from a refrigerator held at −80 °C, activated by a heat shock of 3 min at 40 °C, and a sample of 1 mg of spores was mixed with water-agar (0.1%) and sprayed onto the plants. The plants are 10−13 days old at the time of infection, depending on their development, as the second leaf must have appeared. Afterward, the plants are wrapped in cellophane bags, kept in darkness and 100% humidity for 24 h, and retransferred to light for another 14 days at 65% humidity in the growth chamber until the first harvest is possible. The plants are grown in a 16/8 h light-dark cycle with 10,000 lx and a temperature cycle of 17 °C during the day and 13 °C at night.

The spores are blown onto the collagen film with a funnel-shaped autoclavable device and a pressurized nitrogen inlet. This procedure mimics the real-world scenario of airborne spores dispersed on the sensing area. In addition, the spore samples intrinsically contain small amounts of other particles, such as dust particles, microfibers, dead (and therefore irrelevant) spores, or bubbles and scratches in the collagen film. As will be discussed in further detail below, this is advantageous for training the Bayesian object filter included in the spore recognition software because training a filter for these artifacts already excludes other airborne particles with similar properties. Nonetheless, including additional nontarget objects with other characteristic properties further improves the specificity of the spore detection algorithm. In comparison to real-world field experiments, the spore density is higher and the variety of other particles is smaller. However, the high number of spores helps to generalize the identification model, while the Bayesian object filter can be retrained at any point if so far unconsidered particles appear to pass the object filter. Nonetheless, overloading of the samples can also deteriorate the spore detection performance, as particles overlapping the direction normal to the substrate plane cannot be properly separated from a two-dimensional projection representing the focal plane of the imaging system. In addition, spore clusters with a large lateral dimension can also cause problems because they cannot be well separated into individual objects, as will be discussed in further detail below.

2.3. Image Capture, Segmentation, and Analysis

For each sampling point, a color image and a luminescence image are captured by switching between the two illumination modes. The image sensor is controlled by custom Python scripts provided in the data repository. To obtain comparable results, we have fixed all relevant camera settings such as exposure time, color gains, and analogue gain to constant values.

The captured images are processed by a custom-developed image segmentation and analysis algorithm implemented in MATLAB (MathWorks, R2024a), which is available at https://gitlab.kit.edu/kit/aph/AGW/spore-detection-software. The complete and simplified workflows of this software tool are listed in Figure 2.

As shown in Figure 2a, the workflow can be broken down into three main tasks, i.e., the collection of color and luminescence images as discussed, the detection of spores contained in these images via image segmentation and filtering, and finally, the identification of the detected spores via a Bayesian classification model. The spore detection, itself, can be divided into three subtasks. These include (i) an initial image segmentation, which corresponds to the creation of an object mask that addresses each individual object or object cluster by

https://doi.org/10.1021/acsagscitech.5c00836
ACS Agric. Sci. Technol. 2026, 6, 586−598

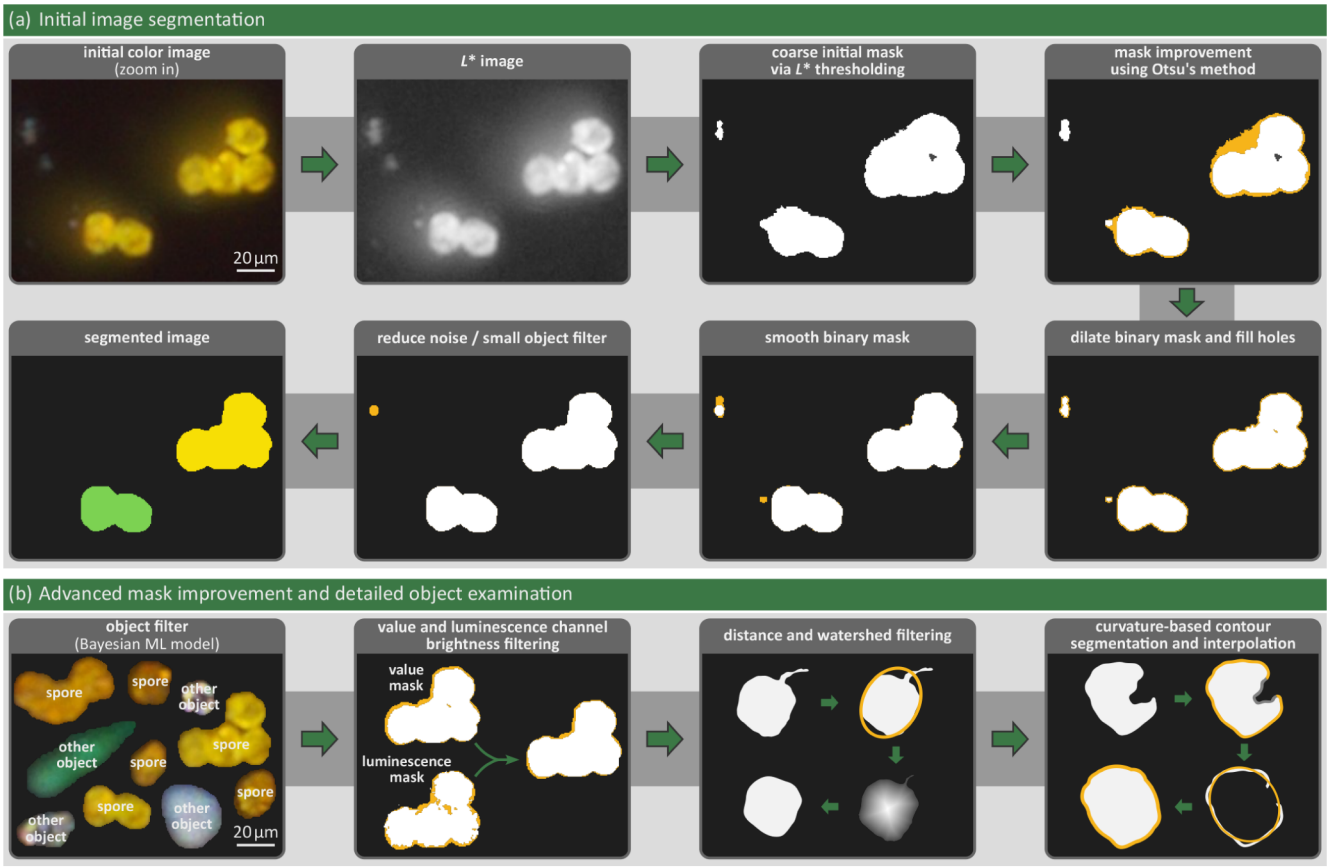

Figure 3. Overview of the segmentation routine applied to color images captured by the sensing unit. (a) The initial image segmentation routine converts an input color image to a labeled object mask. (b) The segmented image is further processed to remove nonspore objects and to correct for more complex artifacts in the individual binary object masks.

a numeric label; (ii) an object filter, which uses a separately trained Bayesian machine learning model (not to be confused with the Bayesian spore identification model) to remove all objects different from spores such as other airborne particles, scratches, bubbles, or other inhomogeneities of the glass substrate or collagen film from the object mask; and (iii) an algorithm to separate individual spores contained in an object cluster.

Concerning the front end of the provided software tool, the algorithm can be divided into four main modes of operation. The first two modes of operation are used to process, segment, and filter the input images. At this stage, the input images must include only a single type of spore, which can be obtained from manually prepared samples as discussed in Section 2.2, but can and should include additional nontarget objects. In the following, we refer to elements of this image type as "class-labeled images". All required user input parameters (30 in this case) can be set via a graphical user interface or by loading a recipe file. A recipe file containing the default parameters used in this study is provided via the mentioned repository.

When operated in the first mode, the software tool exports cropped images of all objects detected by the algorithm and uses a pretrained but nonoptimized object filter to sort them (more or less accurately) into two classes, i.e., a "spores" class and an "other objects" class. By manually relabeling the incorrectly presorted image segments, the object filter, i.e., the underlying Bayesian classification model, was retrained to remove unwanted objects with higher accuracy. In general, training of the object filter can be performed with any kind of distraction particle or imaging artifact by means of a separate software tool that is provided via the same repository mentioned above. The training, validation, and testing follow the same protocol as used for the Bayesian spore identification model that will be discussed in detail in Section 3.

Using the second mode of operation, the detected objects are not exported as image segments but are processed by the object filter. Hence, if the object filter performs well, then only spores and spore clusters remain. This is an important aspect, as the final Bayesian identification model is trained to distinguish spores and therefore does not properly handle objects different from spores. Thereafter, the algorithm extracts characteristic properties from the remaining objects, which are subsequently exported to a so-called spore data set and analyzed statistically. The third mode of operation is utilized to combine the spore data sets of two or more species to train and export a Bayesian classification model. The fourth and last mode of operation is used for inference, where the trained Bayesian model classifies the detected spores using the segmentation algorithm and filters. Hence, the first three modes are used in advance to train the object and identification models and to fine-tune the processing parameters to the given conditions and target objects, while the fourth mode is the mode used for all actual characterization and identification experiments.

In the following, the spore detection algorithm is discussed in more detail. The first steps of this algorithm are visualized in Figure 3a with a captured and cropped image of wheat yellow rust spores. To generate an initial segmented object mask, a brightness filter coarsely removes the dark background caused by dark-field reflection illumination. To do so, the input color image is converted to the CIELAB color space and the L^* channel is binarized. It is important that this initial filter is kept coarse to prevent spores from being overlooked, as the considered spore species appear with different brightness levels. To improve the initial binary mask, we apply an Otsu filter to each individual object. As larger objects or object clusters result in a brighter halo and comatic artifacts, i.e., a directional glow orientated toward the edges of the field of view, the determined Otsu threshold is fine-tuned by an object-size-dependent correction

https://doi.org/10.1021/acsagscitech.5c00836
ACS Agric. Sci. Technol. 2026, 6, 586−598

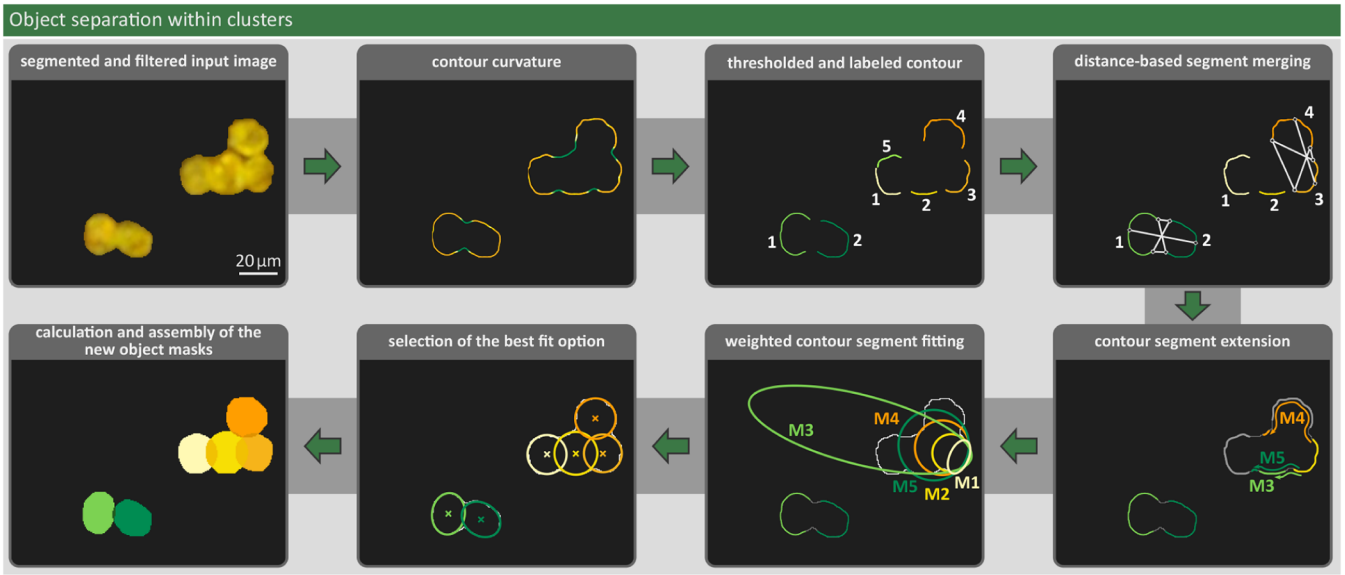

Figure 4. Algorithm workflow to separate spores within clusters. The contour of the mask is segmented by calculating and thresholding the curvature at each point. Each contour segment is artificially extended by either merging it with the previous segment label (M3) or by combining it with the removed center points between the next and the second higher label (M4) or the removed center points between the previous and second previous label (M5). Then, an ellipse (M1) and a circle (M2) are fitted to the initial segment as well as ellipses fitted to the three artificially extended contours (M3−M5). The best fit option is selected by an optimization score.

factor. In the next step, the individual object masks are dilated to close small holes, notches, and cavities. The remaining holes within the object masks are filled in a separate step. Subsequently, the masks are eroded by a few pixels to smooth the contours by removing spikes and other sharp protrusions. In the last step, small object masks that usually stem from noise or nonspore-like objects are removed. The result is a collection of labeled individual object masks that already represent the objects in the input image in a decent way.

For most objects, these initial masks are already sufficient. However, there are also special cases, which will be discussed in the following, that need to be tackled with more advanced tools. These additional steps are illustrated in Figure 3b. First, we apply the already mentioned Bayesian object filter to all separated objects that is designed to remove all objects different from spores from the mask. This is necessary because the optical engine also captures other objects, which can be other airborne particles or even light-scattering bubbles or scratches in the collagen film on the entrance window. Some of these objects can be clearly distinguished from spores by their atypical size, color, or shape, as is the case for dust fibers, for example. However, the sentinel unit may also collect particles with certain visual similarities to wheat rust spores. For this reason, the object filter is implemented as a pretrained Bayesian model that analyzes a variety of geometric and color-related properties of the object as a whole, but also compares differences between the inner and outer parts. The latter features are especially helpful to remove bubbles due to the angle-dependent light reflection. Due to the large variety of airborne particles, which also vary strongly depending on regional and local environmental factors and cannot all be covered in this study, the provided object filter should be understood as the first step of an iterative training approach. Even though there is an "optional safety net filter" that allows the user to filter decisions made by the final spore identification model that fall below a user-defined posterior probability threshold, filtering objects by the Bayesian object filter is much more elegant and effective. If local experiments discover additional or other airborne particles that are not already filtered but should be removed by the object filter, the corresponding Bayesian classification model can and should therefore be retrained by means of the provided software tools, which are designed to allow for a user-friendly adaptation to the local conditions. Additional details on the model and features used can be found in Supplementary Note 2 in the Supporting Information.

In an additional step, the so far unused luminescence channel is considered for improving the object mask. In addition, the initial RGB color image is transformed to the HSV (hue saturation value) color space, and the corresponding value channel is extracted. By combining and comparing thresholds applied to the value and luminescence channels of the considered image, the object masks can be further improved. This filter is particularly helpful to smooth the outline of large objects or spore clusters by, in contrast to the subtractive smoothing filter used before, adding incorrectly removed contour pixels back in. To remove remaining spikes, which usually stem from spores overlapping with scratches in the collagen film or, in rare cases, the development of first germ tubes, we apply a distance transform and watershed filter to selected objects. The objects are selected for watershed analysis if there is a strong deviation between the object mask and a reference ellipse fit of the object. In a last step, large notch artifacts caused by the previously applied filtering steps are removed that occur in some rare cases, especially for spores appearing darker than average. This is done by calculating the curvature of the object contour at every point to extract prominent concave segments. The algorithm removes these contour segments and interpolates them by using an ellipse fit. The combination of this ellipse fit and the input mask yields the final binary object mask.

So far, we have treated individual spores and spore clusters in the same way. It is important, however, that the spore clusters are separated into individual objects before they can be further analyzed. Hence, we have developed a separation algorithm that is visually summarized in Figure 4. The algorithm converts the segmented and filtered input image to a contour curvature map, the same way as is done to remove notches by calculating the curvature at each point on the considered object contour. If the contour curvature falls below a predefined threshold, then the corresponding contour segment is removed. In this context, a threshold value of −0.018 is used, which was determined empirically but has to be a small negative number close to zero in order to select concave contour segments. The remaining contour segments are labeled counterclockwise. Subsequently, all segments are individually checked following different criteria, since the outline of a single spore can contain more than one labeled segment.

As suggested by Lei et al.,[31] the average Euclidean distance between characteristic points on two independent segments is a very useful measure to decide if these segments should get the same label. These

https://doi.org/10.1021/acsagscitech.5c00836
ACS Agric. Sci. Technol. 2026, 6, 586−598

characteristic points are the first, last, and center points on each contour segment. In addition, we also merge segment labels if they are only separated by a few pixels as it is the case for segments 1 and 5 in the depicted example in Figure 4.

After crosschecking the contour segments, five different methods are used to fit a circle or ellipse to each of the individual segments. The first and second methods (M1 and M2) are simple ellipse and circle fits of the current segment. The other three methods (M3−M5) use different extended segments for fitting. For the third method (M3), the current segment is temporarily merged with the previous one, and an ellipse is fitted to the new contour. In contrast, the current segment is extended by the removed center points with high concavity between the next and the second higher label (M4) or by the removed center points between the two previous labels (M5). Hence, we skip one segment label in both cases and add the next contour points with large negative curvature temporarily to the current segment. Subsequently, the algorithm evaluates all five methods by a custom cost function and selects the best option if it does not exceed a critical cost threshold. A high eccentricity is penalized, as well as strong deviations between the area of the fit object and the expected average size of the target spores. In addition, a small overlap between the fit object and the binary mask of the spore cluster is also penalized.

If a proper fit is found, the filled contour segment is combined with the fit object and forms a new object mask. In contrast, the algorithm removes the segment if all five methods do not yield sufficient results. This is usually only the case if the segment does not represent a real spore or if there is too little information for a proper fit, i.e., if the segment has less than approximately five pixels or a vanishingly small convex curvature. All of the resulting object masks of the considered cluster are then added to the collection of single object masks. It should be mentioned that this separation algorithm addresses only objects that contribute to the outer contour of the object cluster. Objects surrounded by other objects in the same cluster cannot be recognized as individual objects. However, experience, especially with real data collected in wheat fields, has shown that larger spore clusters that are more than two spores deep occur only occasionally. In the data sets used in this study, which will be discussed in further detail below, 264 color images with an artificially high spore density were processed. For these images, which contain about 16500 spores, only 12 spores as part of six different spore clusters were missed due to the fact that they did not contribute to the outer contour of the corresponding spore cluster.

The individual object masks are then used to extract geometric, color, and luminescence properties, which are then either used to create a spore data set or passed to the Bayesian classification model for identifying the objects. In both cases, the results are exported and visualized. Then, the next image is loaded for the same processing.

3. RESULTS

For each target species, multiple samples are prepared as described above, and images for model training, validation, and testing are collected under both illumination conditions at different positions on the film. For this study, we recorded a total of 528 images, half of the images taken under white-light illumination, and the other half captured using the UV mode of the incorporated illumination unit. Half of the color images, i.e., 132 pictures, and the corresponding 132 luminescence images were captured at different positions on three class-labeled but independent wheat yellow rust samples. The other half of the images were taken under the same conditions, but on three independent wheat brown rust samples. Following the common routine, half of the images are used for training the identification model, while the remaining half is distributed equally among the validation and testing data sets. Each data set is assembled using an equal number of images from both spore types and from every independent sample. A visual representation of this allocation of pictures can be found in Figure S3 in the Supporting Information. On average, each image contains about 49 spores of wheat yellow rust and approximately 78 spores of wheat brown rust, resulting in an average spore density of approximately 13.5 spores/mm^2 for yellow rust and about 22.3 spores/mm^2 for brown rust samples. These spore densities, however, strongly depend on the samples from which the images are collected. They vary between 3 spores/mm^2 and 31 spores/mm^2. For this reason, images from different samples are used in all data sets to represent both cases of low and high spore density. In total, we have imaged more than 8600 spores for training (*Pst*: 3247, *Pt*: 5386), about 4400 for validation (*Pst*: 1547, *Pt*: 2874), and approximately 3700 for testing (*Pst*: 1633, *Pt*: 2057).

For training the two Bayesian classification models, a long list of features is extracted from the objects contained in the segmented images. These features mainly contain properties that are extracted from the cyan, magenta, yellow, and key color channels. The features are extracted from the CMYK color space, as the spores are expected to produce a bright signal in the yellow channel due to their characteristic yellow and brown colors. In addition, we use geometric properties, the lightness L^* channel, calculate a brightness gradient map, and use the separately captured luminescence channel. Typical statistical quantities, such as the arithmetic mean, standard deviation, skewness, kurtosis, and Shannon entropy, are calculated for all pixels of the currently analyzed object as well as in certain interesting regions, such as the center and perimeter regions. Additional information on the feature extraction as well as a full list of all the features considered can be found in Supplementary Note 2 in the Supporting Information.

During model training, we use a minimum-redundancy-maximum-relevance (mRMR) algorithm[54] to sort the extracted features according to their importance for the decision process. To avoid overfitting and underfitting, the model is trained multiple times following a typical iterative validation routine. In the first step, the model is trained with the training data set, while only the most relevant feature according to the mRMR analysis is considered in the process. Using the independent validation data set, we evaluate the performance of the trained model by determining the corresponding confusion matrix and calculating the established scores: precision, accuracy, sensitivity, specificity, the balanced and unbalanced F_1 score, and the G-mean score as performance metrics. For the sake of clarity and reproducibility, additional details on these metrics can be found in Supplementary Note 4 in the Supporting Information. In each consecutive iteration step, the next remaining most relevant feature is added to the list of considered features, the Bayesian model is retrained, and the performance of the temporary model is characterized using the same validation data set and performance scores. Therefore, all extracted features are considered in the last iteration step. Finally, the best iteration step, i.e., the best performing model and feature combination, is selected to reduce the generalization error to its minimum. To have a measure that is symmetric under commutation of the classes, we select the set of features that yields the highest G-mean score, i.e., the geometric mean of sensitivity and specificity.

To train the Bayesian object filter, all objects are considered, i.e., not only spores but everything else that is also selected by the unfiltered object mask including dust particles and fibers, other biological particles due to small levels of contamination

https://doi.org/10.1021/acsagscitech.5c00836
ACS Agric. Sci. Technol. 2026, 6, 586−598

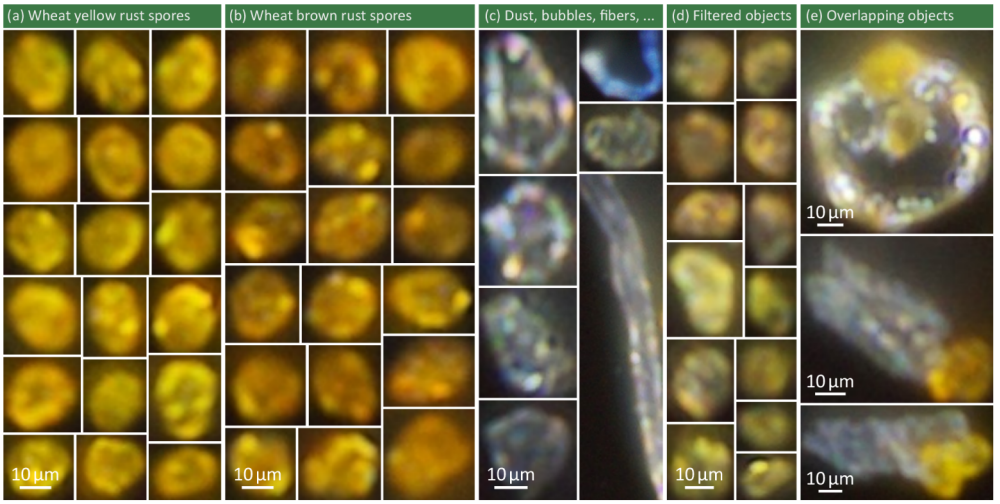

Figure 5. Typical image segments as extracted by the provided software tools from the testing data sets. (a) Collection of typical yellow rust (*Pst*) spore images. (b) Typical images of brown rust spores (*Pt*) as extracted by the algorithm. (c) Typical images of bubbles, notches, scratches, and fibers in and on the collagen film. (d) Objects with geometric and color-related properties similar to wheat rust spores that were filtered by the Bayesian object filter. (e) Incorrectly filtered spores as they are covered or in contact with other objects that contribute more pixels to the spore-object cluster, hence impeding a correct classification.

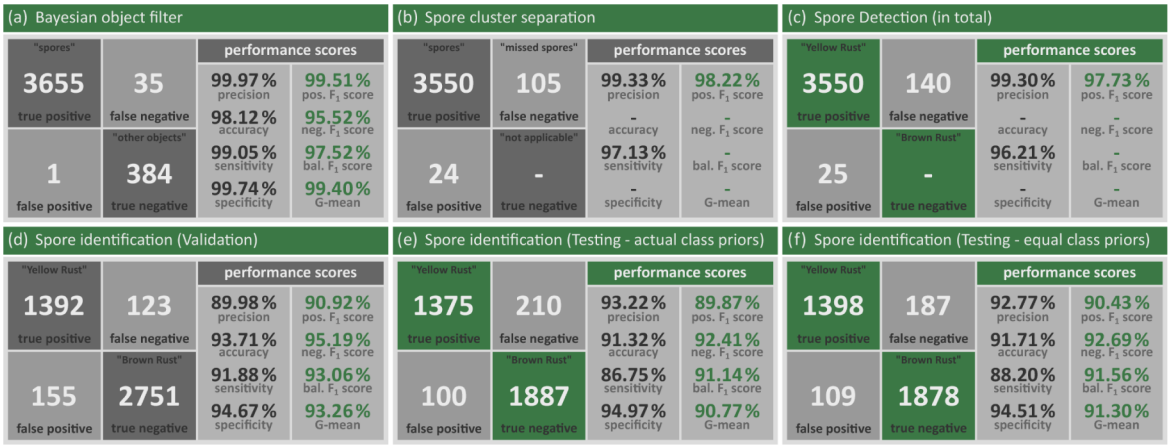

Figure 6. Performance scores of the spore recognition algorithm and features used for the Bayesian identification model. (a) Confusion matrix and performance scores of the object filter classifying objects into target spores and other objects. (b) Performance scores of the routine used to separate spores within clusters. As an appropriate definition of false negatives is not possible in this case, related metrics such as the accuracy and specificity cannot be calculated. (c) Confusion matrix and total performance scores of the image segmentation, which are calculated from the metrics of the object filter and the spore separation routine. (d) Performance scores and confusion matrix of the spore identification when classifying urediniospores with the presented Bayesian model with validation feedback. (e), (f) Performance of the trained Bayesian identification model for unseen images with priors calculated based on the number of spores during training and with equalized priors for each class.

of the spore samples, and image artifacts caused by scratches or bubbles in the collagen film. These training objects are labeled as "spores" or "other objects". Typical images of these spores and other objects are depicted in Figure 5. In panels a and b of Figure 5, typical images of yellow and brown rust spores are shown as detected and cropped by the presented algorithm. Segmented images of typical "other" objects contained in the training, validation, and testing data sets are shown in panels c and d of Figure 5. Please note that only objects with reasonable sizes are shown. Objects that are much smaller or significantly larger than typical wheat rust spores are automatically filtered and are not of interest for this discussion. Figure 5c shows typical bubbles, notches, scratches, and dust fibers, as they can be often observed in or on the collagen films. The objects depicted in Figure 5d are more interesting because they have a highly similar yet still different visual appearance compared to wheat rust spores. These particles are most likely dead or deteriorated spores or other biological particles of unknown type. Therefore, these particles are used to analyze the specificity of the Bayesian object filter, as will be discussed below.

To train the Bayesian identification model, class-labeled images of yellow and brown rust spores are used as proof-of-concept. However, both Bayesian models still offer the possibility of being retrained with updated data sets including other or additional target or nontarget particles. Under our conditions, the smaller size limit of these particles is restricted by the mask smoothing function and cluster separation routine. We estimate a size limit of approximately 5 μm. Particle masks smaller than that will be eroded by the smoothing filter or cannot be processed by the cluster separation routine.

https://doi.org/10.1021/acsagscitech.5c00836
ACS Agric. Sci. Technol. 2026, 6, 586−598

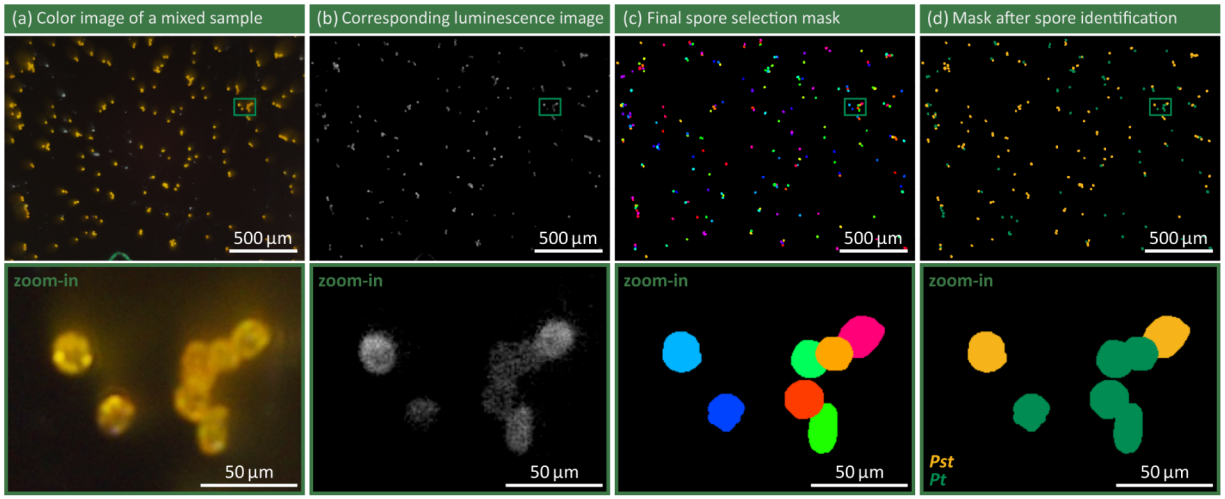

Figure 7. Results of a validation experiment using images that were captured with the presented optical engine from mixed spore samples. The first row depicts the full images or object masks, while the second row shows zoomed-in versions of the same images/masks but cropped by the green rectangles. (a) Example of a captured color image containing yellow rust spores, brown rust spores, and a small level of contamination from dust particles, bubbles, scratches, and dead spores. (b) Corresponding luminescence image, here contrast-optimized for better visualization. (c) Final spore selection mask after the spore cluster separation routine and final filtering steps. The different colors are arbitrary color labels to visualize the different individual object masks. (d) Object mask labeled by the Bayesian identification model colorized in yellow (*Pst*) and green (*Pt*) to visualize the classification outcomes.

We use the class-labeled testing data sets containing entirely unseen images to characterize the performance of the spore detection, i.e., the Bayesian object filter and the separation algorithm for objects within clusters and the spore identification. By comparison of each step of the algorithm with a manual analysis of the images contained in the testing data sets, the performance of each individual subfunction has been analyzed. For the sake of brevity and clarity, the analysis of smaller subfunctions is merged with the outcomes of the Bayesian object filter or the cluster separation routine in this discussion. Hence, everything referring to the characterization of the Bayesian object filter also includes all subfilters applied previous to the object filter. Accordingly, all subfunctions applied after the Bayesian object filter are merged with the analysis of the cluster separation routine. This is possible since all subfunctions except for the object filter and cluster separation are designed as highly specific mask improvement tools that only occasionally select or exclude spore-like objects. Following this simplified characterization routine, we use typical confusion matrices and the introduced performance metrics when applicable. The resulting confusion matrices and scores are shown in Figure 6a–f. A detailed analysis of all individual subfunctions can be found in Supplementary Table S3 and Supplementary Note 5 in the Supporting Information.

The characterization of the Bayesian object filter, as depicted in Figure 6a, yields a high G-mean score of approximately 99.4% and a positive class F_1 score of about 99.5%, effectively separating target spores from other particles including the particles shown in Figure 5c and d. As can be seen in Figure 6a, only one nonspore particle was able to pass the Bayesian object filter, while 384 objects were correctly removed together with an uncountable number of particles and background pixels much smaller than the typical size of wheat rust spores. The spore-cluster-separation algorithm, summarized in Figure 6b, yields a slightly lower but still high F_1 score of 98.2% for the positive class. The cluster separation algorithm is technically not a binary classification problem. Nonetheless, we can use the same concepts to characterize the performance of the corresponding tools. However, we omit all related scores to avoid inconclusive metrics, as each correctly removed background pixel could be counted as a true negative result.

When the object filter, cluster separation, and all smaller subfunctions are combined, the spore detection can be characterized holistically, as depicted in Figure 6c, yielding a positive class F_1 score of 97.7%. As shown in Figure 6d and e, the spore identification, using the 13 most relevant features and the actual class priors p_{Pst} = 0.376 and p_{Pt} = 0.624 as automatically calculated from the number of considered spores during training, yields a G-mean score of 93.3% with validation feedback or approximately 90.8% for the entirely unseen testing data, which is lower than the other scores but still sufficiently large for the presented application. Using equalized priors, i.e., p_{Pst} = p_{Pt} = 0.5, the G-mean score can be slightly increased to 91.3%, as can be seen in Figure 6f. Both descriptions have valid arguments, so the provided software allows for selecting between both options. With a generalization gap of 1.49% and 1.96% between validation and testing regarding the balanced F_1 score and the G-mean score, respectively, the identification model generalizes well toward unseen spore images.

Even though the Bayesian classification models were validated and tested with unseen data sets, we performed an independent validation experiment using mixed spore samples, i.e., images collected from samples containing yellow rust spores, brown rust spores, and a small level of contamination with dust particles, dead spores, bubbles, scratches, etc. When one of these images is randomly selected and processed with the provided software tools, the results shown in Figure 7 have been obtained. As described above, the initial color and luminescence images, which are shown in panels a and b in Figure 7, are combinedly segmented, filtered, and cluster-separated, resulting in the final spore selection mask depicted in Figure 7c. Using this selection mask, the remaining objects are identified as either yellow or brown rust spores, as depicted in Figure 7d. When compared to a manual analysis of the image, the spore detection yields, with a true positive value of

https://doi.org/10.1021/acsagscitech.5c00836
ACS Agric. Sci. Technol. 2026, 6, 586−598

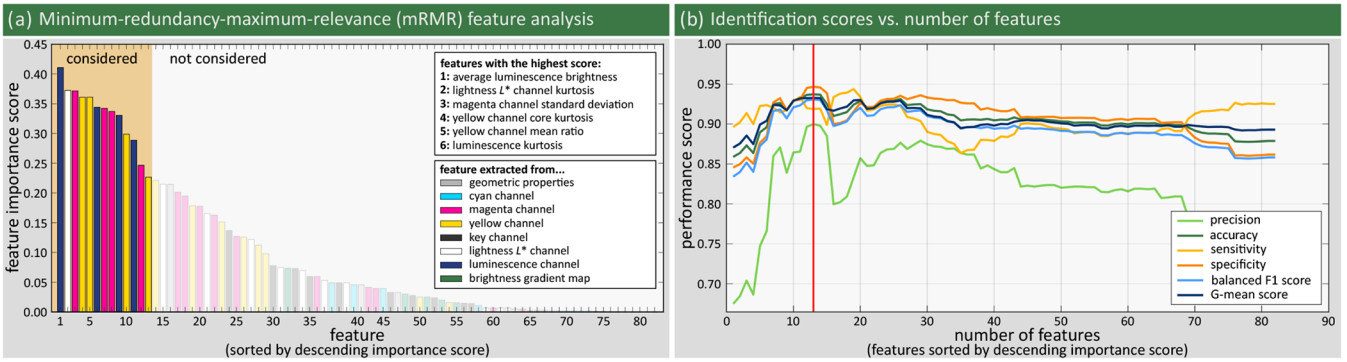

Figure 8. Feature analysis and Bayesian model validation. (a) Importance score of all extracted spore features calculated by using a minimum-redundancy-maximum-relevance (mRMR) approach. (b) Performance of the Bayesian identification model in dependence of the number of considered features sorted by their importance scores shown in (a).

204, a false positive value of 2, and a false negative value of 11, a precision of 99.0%, a specificity of 94.9%, and a positive-class F_1 score of 96.9%. The spore identification cannot be analyzed that easily as the samples are mixed and therefore not labeled. However, when calculating the posterior probabilities using the trained and provided Bayesian identification model, only 28 out of 204 spores, i.e., in 13.73% of the cases, cannot be sorted into one of the two spore classes with a corresponding class affiliation probability below 95.45% (2σ interval). Similarly, only 6 out of 204 spores, i.e., 2.94% of the cases, cannot be identified with a posterior probability larger than 68.3%, i.e., within the 1σ interval. Hence, the presented tools yield a high detection and identification performance even under challenging conditions where two types of objects with highly similar color and geometric properties appear together, so that it is already difficult for the human eye to distinguish them. An unreasonably high overconfidence of the identification model can be excluded when considering the results from the training, validation, and testing routines discussed above. As shown for one example in the zoomed-in pictures in Figure 7, this classification even works well for mixed spore clusters, where all of the shown spores except for one were identified with a maximum posterior probability exceeding 99.5%. The single challenging decision for the spore with the largest overlap to its neighboring particles still resulted in a posterior probability of 73.9%.

4. DISCUSSION

Object identification and filtering via Bayesian classifiers instead of, for example, deep learning approaches were chosen for this application as the trained models are simply built upon a set of statistical quantities, such as the mean values and standard deviations of the corresponding feature-related probability distributions obtained during the model training. Therefore, Bayesian classifiers are very fast and especially memory-efficient while still reaching high classification scores even for comparably small training data sets of only a few hundred objects. However, the most important reason why Bayesian classification was selected is the fact that all of the steps are interpretable. Hence, each decision can be assessed and understood such that one can learn more about the particles considered and their characteristic properties. In addition, features can be systematically selected by their relevance, which makes the decision process significantly more robust against irrelevant features. In the following, these advantages are discussed in the context of the presented study.

To optimize the performance of two Bayesian classification models, an mRMR feature analysis is used, as mentioned above. The corresponding results for training the spore identification model are shown in Figure 8. This result is particularly interesting as we can directly assess which features are relevant to differentiate urediniospores of the wheat yellow and brown rust fungi. As can be seen, the most relevant feature is the average luminescence brightness, i.e., a feature that can be accessed only because the presented spore sentinel unit is equipped with an illumination unit that can be switched between white-light and UV illumination. In addition to the average luminescence brightness, the most important features are all extracted from either the luminescence, yellow, magenta, or L^* channel. The other color channels and the geometric properties are less relevant for distinguishing the target spores but can, for example, still be relevant for the Bayesian object filter or if the identification model is retrained for additional or other target particles. In the presented case, the maximum G-mean score is reached for the identification model if the 13 most important features are considered, as shown in Figure 8b. A full list of all considered and unconsidered features can be found in Table S2 in Supplementary Note 2. When training the Bayesian object filter, entirely different features become relevant. One example of an object filter training and the corresponding results from the mRMR analysis can also be found in Supplementary Note 2.

This means that omitting luminescence images from the analysis would degrade the classification scores. Likewise, omitting other considered features connected to the color images would also deteriorate the classification scores. We here follow the most systematic path, i.e., considering as many features as possible and selecting the most important ones by means of the discussed mRMR algorithm. These most important features are highlighted by the orange background in Figure 8a.

We note in passing that collecting luminescence images requires exposure times for the image sensor of several hundred milliseconds. Hence, a proper shutter solution in front of the entrance window is required to reduce the influence of background light that is transmitted or scattered through the optical imaging system. This additional shutter also improves the image contrast when collecting color images in daylight.

In addition to the time required for image collection and data transfer, which can be conservatively estimated to a few seconds, the image processing time is about one minute per image set if performed on a standard server CPU (Intel Xeon

https://doi.org/10.1021/acsagscitech.5c00836
ACS Agric. Sci. Technol. 2026, 6, 586−598

Platinum 8260) including generating and plotting of several control figures. Here, one image set refers to the combination of a color image and the corresponding luminescence image. Therefore, the sampling time can even be reduced below one minute if the central computation unit is replaced with better performing hardware, if the software code is executed without generating control figures, or if the algorithm is further optimized for better runtime performance.

As indicated by the confusion matrix shown in Figure 6a, the Bayesian object filter has a slight bias toward missing a few spores. Nevertheless, it effectively removes nonspore-like objects as only one is incorrectly classified. The missed spores mainly stem from mixed spore-object clusters, where the spores are in contact with other objects or (partially) covered by them. Examples of such spore-object clusters that have been removed by the Bayesian object filter are depicted in Figure 5e. In such cases, the characteristic properties of the affected spores are corrupted by the feature values of the other object, especially if the corresponding object covers a larger proportion of the shared object mask, which then results in incorrect decision outcomes by the object filter.

The final cluster separation algorithm also shows a slight bias toward missing spores in clusters. This small bias is caused by an insufficiently low number of pixels contributing to certain contour segments, which then results in inaccurate contour fits. As mentioned earlier, this is typically the case if the contour segments contain less than approximately five pixels or if they have a vanishingly small convex curvature. Nevertheless, both tools combined still result in precise and sufficiently sensitive spore detection.

Even though the identification model takes more object features for the decision process into account, it still results in lower performance scores due to a non-negligible number of misclassifications. These false positives and false negatives are caused by the overlap of the probability distributions that characterize the features of the two target classes. However, the achieved identification scores are still fully sufficient for the presented application. In addition, wheat yellow and brown rust spores were intentionally chosen for this proof-of-concept study since they have a very similar appearance at the single-spore level and are already difficult to distinguish for the trained eye in low-magnification images.

In conclusion, we presented a sensing method that uses optical imaging in combination with a custom machine learning algorithm to detect and identify airborne urediniospores of wheat rust fungi to monitor and forecast the spread of wheat rust diseases. With the presented spore sentinel unit and the corresponding software tools, we were able to achieve spore detection scores greater than 96.2% and spore identification scores between 88.2% and 94.5%. In the present study, wheat yellow rust (stripe rust) and wheat brown rust (leaf rust) have been selected for proof-of-concept experiments, as urediniospores of these fungi have a very similar appearance and as they also have a significant impact on global wheat production.

We showed that it is highly beneficial to collect and analyze luminescence data to support the identification process by considering new characteristic features, in addition to regular object properties extracted from color images. These luminescence features are accessible by including a custom illumination unit in the imaging system that can be operated in both a white-light and an ultraviolet reflection-based dark-field-like illumination mode.

The main advantage of the presented sensing method is its flexibility to be optimized for varying conditions and target spores. In this context, the presented results can be understood as a first step in an iterative routine that is used to update and retrain the machine learning models, for example, to extend the database of nontarget particles or spores. In addition, the presented and published software tool can be retrained and reoptimized with reasonable effort to target additional or entirely different airborne spores so that also other fungal crop diseases can be monitored. This, however, may also require a reevaluation and adjustment of some of the mentioned 30 image processing parameters defined by the user or extracted from a recipe file. Including wheat black rust (stem rust) spores in the identification model, for example, is a reasonable next step, and high identification scores are expected as urediniospores of wheat black rust have a different appearance compared to the wheat yellow and brown rust spores.

If multiple sentinel units are wirelessly interconnected, additional data related to the ambient conditions such as wind, temperature, weather, etc. can be combined with the position data of the sentinel units and used to simulate and forecast the spread of the underlying crop disease. Hence, a network of these sentinel units acts as a cost-effective early warning system for wheat rusts and other fungal crop diseases. On this basis, time- and cost-effective countermeasures can be initiated.

■ ASSOCIATED CONTENT

Data Availability Statement

Exemplary data used for this paper can be found on a public data repository available under https://doi.org/10/35097/qcvcy4151nqdd677. Full data will be provided upon reasonable request.

Supporting Information

The Supporting Information is available free of charge at https://pubs.acs.org/doi/10.1021/acsagscitech.5c00836.

Details on the optical imaging system, details on the Bayesian classification models, a visual overview of the utilized data sets, metrics used to characterize the main functions of the presented algorithm, and a detailed analysis of the performance of the spore detection tools and filters are covered (PDF)

■ AUTHOR INFORMATION

Corresponding Authors

Sebastian Kalt − *Institute of Applied Physics (APH), Karlsruhe Institute of Technology (KIT), Karlsruhe 76131, Germany;* orcid.org/0009-0004-8848-8991; Email: sebastian.kalt@kit.edu

Martin Wegener − *Institute of Applied Physics (APH), Karlsruhe Institute of Technology (KIT), Karlsruhe 76131, Germany; Institute of Nanotechnology (INT), Karlsruhe Institute of Technology (KIT), Karlsruhe 76131, Germany;* Email: martin.wegener@kit.edu

Authors

Berthold Wegner − *EU Imaging, Sensing, and Perception Center, Sony Semiconductor Solutions Europe, Sony Europe Ltd., Stuttgart 70372, Germany*

Max Strauß − *EU Imaging, Sensing, and Perception Center, Sony Semiconductor Solutions Europe, Sony Europe Ltd., Stuttgart 70372, Germany*

Lenon Romano Modesto − *EU Imaging, Sensing, and Perception Center, Sony Semiconductor Solutions Europe, Sony Europe Ltd., Stuttgart 70372, Germany*
Tim Alletzhäusser − *Institute of Applied Physics (APH), Karlsruhe Institute of Technology (KIT), Karlsruhe 76131, Germany*
Philipp Schulz − *Federal Research Center for Cultivated Plants, Institute for Plant Protection in Field Crops and Grassland, Julius Kühn-Institut (JKI), Kleinmachnow 14532, Germany*
Tzenka Miteva − *EU Imaging, Sensing, and Perception Center, Sony Semiconductor Solutions Europe, Sony Europe Ltd., Stuttgart 70372, Germany*

Complete contact information is available at: https://pubs.acs.org/10.1021/acsagscitech.5c00836

Author Contributions

S.K. worked on optical design, hardware assembly, data collection, and the spore detection and identification algorithm. B.W., L.R.M., and M.S. supported the work on the imaging unit, hardware assembly, and data collection. L.R.M., B.W., and T.M. prepared the spore samples for data collection, supported by S.K. P.S. provided the spores used for all lab experiments and T.A. helped with the machine-learning tools. M.W. and T.M. supervised the project and gathered its funding. S.K. drafted an initial version of the manuscript. All authors contributed to the writing of the manuscript and have given approval to the final version.

Funding

S.K. and M.W. acknowledge funding by the Deutsche Forschungsgemeinschaft (DFG, German Research Foundation) under Germany's Excellence Strategy via the Excellence Cluster "3D Matter Made to Order" (EXC-2082/1-390761711), by the Carl Zeiss Foundation, and by the Helmholtz program Materials Systems Engineering.

Notes

The spore-detection-and-identification script is published under the MIT software license and can be accessed via https://gitlab.kit.edu/kit/aph/AGW/spore-detection-software. The authors declare no competing financial interest.

■ ACKNOWLEDGMENTS

The authors thank Michael Hippe, Werner Gilde, and Maik Nothdurft (KIT) for their technical support as well as Jannis Weinacker and Pascal Kiefer (KIT) for stimulating discussions. In addition, the authors thank Frank Scholz (Sony) for his help with preparing reference samples.

■ ABBREVIATIONS

Pst, *Puccinia striiformis* f.sp. *tritici* (wheat yellow rust/wheat stripe rust); *Pt*, *Puccinia triticina* (wheat brown rust/wheat leaf rust); CMOS, complementary metal-oxide semiconductor; PCB, printed circuit board; SMD, surface-mounted device; LED, light-emitting diode; UV, ultraviolet; ML, machine learning; mRMR, minimum-redundancy-maximum-relevance

■ REFERENCES

(1) Golan, J. J.; Pringle, A. Long-Distance Dispersal of Fungi. *Microbiol. Spectrum* **2017**, *5*, 309−333.
(2) Meyer, M.; Thurston, W.; Smith, J. W.; Schumacher, A.; Millington, S. C.; Hodson, D. P.; Cressman, K.; Gilligan, C. A. Three-Dimensional Visualization of Long-Range Atmospheric Transport of Crop Pathogens and Insect Pests. *Atmosphere* **2023**, *14* (6), 910.
(3) Hovmøller, M. S.; Yahyaoui, A. H.; Milus, E. A.; Justesen, A. F. Rapid Global Spread of Two Aggressive Strains of a Wheat Rust Fungus. *Mol. Ecol.* **2008**, *17* (17), 3818−3826.
(4) Ali, S.; Gladieux, P.; Leconte, M.; Gautier, A.; Justesen, A. F.; Hovmøller, M. S.; Enjalbert, J.; de Vallavieille-Pope, C. Origin, Migration Routes and Worldwide Population Genetic Structure of the Wheat Yellow Rust Pathogen Puccinia Striiformis f.Sp Tritici. *PLoS Pathog.* **2014**, *10* (1), No. e1003903.
(5) Meyer, M.; Cox, J. A.; Hitchings, M. D. T.; Burgin, L.; Hort, M. C.; Hodson, D. P.; Gilligan, C. A. Quantifying Airborne Dispersal Routes of Pathogens over Continents to Safeguard Global Wheat Supply. *Nat. Plants* **2017**, *3* (10), 780−786.
(6) Zhou, X.; Fang, T.; Li, K.; Huang, K.; Ma, C.; Zhang, M.; Li, X.; Yang, S.; Ren, R.; Zhang, P. Yield Losses Associated with Different Levels of Stripe Rust Resistance of Commercial Wheat Cultivars in China. *Phytopathology* **2022**, *112* (6), 1244−1254.
(7) Wellings, C. R. Global Status of Stripe Rust: A Review of Historical and Current Threats. *Euphytica* **2011**, *179* (1), 129−141.
(8) Beddow, J. M.; Pardey, P. G.; Chai, Y.; Hurley, T. M.; Kriticos, D. J.; Braun, H.-J.; Park, R. F.; Cuddy, W. S.; Yonow, T. Research Investment Implications of Shifts in the Global Geography of Wheat Stripe Rust. *Nat. Plants* **2015**, *1*, 15132.
(9) Chen, X. M. Epidemiology and Control of Stripe Rust [Puccinia Striiformis f. Sp. Tritici] on Wheat. *Can. J. Plant Pathol.* **2005**, *27* (3), 314−337.
(10) Dean, R.; Van Kan, J. A. L.; Pretorius, Z. A.; Hammond-Kosack, K. E.; di Pietro, A.; Spanu, P. D.; Rudd, J. J.; Dickman, M.; Kahmann, R.; Ellis, J.; et al. The Top 10 Fungal Pathogens in Molecular Plant Pathology. *Mol. Plant Pathol.* **2012**, *13* (4), 414−430.
(11) Wan, A. M.; Chen, X. M.; He, Z. H. Wheat Stripe Rust in China. *Aust. J. Agric. Res.* **2007**, *58* (6), 605−619.
(12) *The Cereal Rusts*. Bushnell, W. R.; Roelfs, A. P., Ed.; Academic Press: Orlando, 1984.
(13) Food and Agriculture Organization of the United Nations (FOA), *Crops And Livestock Products*: 2024, accessed 2024−10−07. https://www.fao.org/faostat/en/#data/QCL.
(14) Savary, S.; Willocquet, L.; Pethybridge, S. J.; Esker, P.; McRoberts, N.; Nelson, A. The Global Burden of Pathogens and Pests on Major Food Crops. *Nat. Ecol. Evol.* **2019**, *3* (3), 430−439.
(15) Chen, W.; Wellings, C.; Chen, X.; Kang, Z.; Liu, T. Wheat Stripe (Yellow) Rust Caused by Puccinia Striiformis f. Sp. Tritici. *Mol. Plant Pathol.* **2014**, *15* (5), 433−446.
(16) Bolton, M. D.; Kolmer, J. A.; Garvin, D. F. Wheat Leaf Rust Caused by Puccinia Triticina. *Mol. Plant Pathol.* **2008**, *9* (5), 563−575.
(17) Wang, M.; Chen, X. Stripe Rust Resistance. In *Stripe Rust*. Chen, X.; Kang, Z.; SpringerDordrecht: Netherlands, 2017; pp. 353−558. .
(18) Hafez, Y.; Mazrou, Y.; Shahin, A.; Mehiar, F.; Eid, M.; Abdelaal, K. Yield Losses in Wheat Genotypes Caused by Stripe Rust (Puccinia Striifarmis f. Sp. Tritici) in North Delta, Egypt. *Not. Bot. Horti Agrobot. Cluj-Napoca* **2022**, *50* (2), 12622−12622.
(19) Porras, R.; Miguel-Rojas, C.; Pérez-de-Luque, A.; Sillero, J. C. Macro- and Microscopic Characterization of Components of Resistance against Puccinia Striiformis f. Sp. Tritici in a Collection of Spanish Bread Wheat Cultivars. *Agronomy* **2022**, *12* (5), 1239.
(20) Schwessinger, B. Fundamental Wheat Stripe Rust Research in the 21st Century. *New Phytol.* **2017**, *213* (4), 1625−1631.
(21) Liu, W.; Frick, M.; Huel, R.; Nykiforuk, C. L.; Wang, X.; Gaudet, D. A.; Eudes, F.; Conner, R. L.; Kuzyk, A.; Chen, Q.; Kang, Z.; Laroche, A. The Stripe Rust Resistance Gene *Yr10* Encodes an Evolutionary-Conserved and Unique CC−NBS−LRR Sequence in Wheat. *Mol. Plant* **2014**, *7* (12), 1740−1755.
(22) Thach, T.; Ali, S.; Justesen, A. F.; Rodriguez-Algaba, J.; Hovmøller, M. Recovery and Virulence Phenotyping of the Historic 'Stubbs Collection' of the Yellow Rust Fungus Puccinia Striiformis from Wheat. *Ann. Appl. Biol.* **2015**, *167* (3), 314−326.

(23) Wu, X. X.; Lin, Q. J.; Ni, X. Y.; Sun, Q.; Chen, R. Z.; Xu, X. F.; Qiu, Y. C.; Li, T. Y. Characterization of Wheat Monogenic Lines with Known Sr Genes and Wheat Lines with Resistance to the Ug99 Race Group for Resistance to Prevalent Races of Puccinia Graminis f. Sp. Tritici in China. *Plant Dis.* **2020**, *104* (7), 1939−1943.
(24) Zhang, X.; Huang, L.; Tang, W.; Qiu, A.; Li, X.; Zhou, X.; Yang, S.; Wang, M.; Chen, X.; Chen, W.; et al. Virulence Characterization of Wheat Stripe Rust Population in China in 2023. *Plant Pathol.* **2024**, 363−377.
(25) Hajam, M.; Wani, M.; Rather, A. *Agriculture Science: Research And Review VII*. 2022, Bhumi.
(26) Elsharkawy, M. M.; Omara, R. I.; Mostafa, Y. S.; Alamri, S. A.; Hashem, M.; Alrumman, S. A.; Ahmad, A. A. Mechanism of Wheat Leaf Rust Control Using Chitosan Nanoparticles and Salicylic Acid. *J. Fungi* **2022**, *8* (3), 304.
(27) Zerihun, A. A.; Abebele, G. M. Evaluation of Fungicides Efficacy for the Control of Yellow Rust (Puccinia Striiformis f.s.Tritici) Disease on Bread Wheat, Arsi Highlands of Ethiopia. *Asian J. Res. Agric. For.* **2024**, *10* (4), 482−488.
(28) Mahmoodi, S.; Ganje, M. B.; Ahmadi, K.; Dalvand, Y.; Naghibi, A.; Newlands, N. K. Modeling Spatiotemporal Distribution of Yellow Rust Wheat Pathogen Using Machine Learning Algorithms: Insights from Environmental Assessment. *Environ. Technol. Innovation* **2024**, *36*, 103865.
(29) Charaya, M.; Upadhyay, A.; Bhati, H.; Kumar, A. Plant Disease Forecasting: Past Practices to Emerging Technologies. *Plant Dis., Manage. Strategies* **2021**, 1−30.
(30) Doroshenko, O. V.; Golub, M. V.; Kremneva, O. Y.; Shcherban', P. S.; Peklich, A. S.; Danilov, R. Y.; Gasiyan, K. E.; Ponomarev, A. V.; Lagutin, I. N.; Moroz, I. A.; Postovoy, V. K. Automated Assessment of Wheat Leaf Disease Spore Concentration Using a Smart Microscopy Scanning System. *Agronomy* **2024**, *14* (9), 1945.
(31) Lei, Y.; Yao, Z.; He, D. Automatic Detection and Counting of Urediniospores of Puccinia Striiformis f. Sp. Tritici Using Spore Traps and Image Processing. *Sci. Rep.* **2018**, *8* (1), 13647.
(32) Vimala, G. S. A. G.; Arul Raj, A. M.; Bharathi, C. R.Deep Learning-Based Image Processing for Early Detection of Stripe Rust in Wheat Crops Using CNN Model*2024 8th International Conference On Electronics, Communication And Aerospace Technology (ICECA)* IEEE2024162−166
(33) Zhang, J.; Pan, C.; Liu, S.; Kou, Y.; Tang, J.; Wang, Y.; Yang, N.; Huang, R. Crop Disease Source Location and Monitoring System Based on Diffractive Light Identification Airborne Spore Sensor Network. *IEEE Internet Things J.* **2021**, *9*, 11030−11042.
(34) Ren, Y.; Huang, W.; Ye, H.; Zhou, X.; Ma, H.; Dong, Y.; Shi, Y.; Geng, Y.; Huang, Y.; Jiao, Q.; Xie, Q. Quantitative Identification of Yellow Rust in Winter Wheat with a New Spectral Index: Development and Validation Using Simulated and Experimental Data. *Int. J. Appl. Earth Obs. Geoinformation* **2021**, *102*, 102384.
(35) Ren, Y.; Ye, H.; Huang, W.; Ma, H.; Guo, A.; Ruan, C.; Liu, L.; Qian, B. A New Spectral Index for the Quantitative Identification of Yellow Rust Using Fungal Spore Information. *Big Earth Data* **2021**, *5*, 201−216.
(36) Jing, X.; Ye, Q.; Chen, B.; Li, B.; Du, K.; Xue, Y. Monitoring of Wheat Stripe Rust Using Red SIF Modified by Pseudokurtosis. *Agronomy* **2024**, *14* (8), 1698.
(37) Yuan, J.; Huang, Z.; Zhang, D.; Yang, X.; Gu, C. SporeDet: A Real-Time Detection of Wheat Scab Spores. In *Advanced Intelligent Computing Technology and Applications*. Lecture Notes in Computer Science, Huang, D.-S.; Premaratne, P.; Jin, B.; Qu, B.; Jo, K.-H.; Hussain, A.; Springer Nature: Singapore, 2023; Vol. *14087*, pp. 531−543. .
(38) Li, K.; Zhu, X.; Qiao, C.; Zhang, L.; Gao, W.; Wang, Y. The Gray Mold Spore Detection of Cucumber Based on Microscopic Image and Deep Learning. *Plant Phenomics* **2023**, *5*, 0011.
(39) Spornado *Early Alert System For Crop Disease*, Spornado Sampler; accessed 2024−10−24, https://spornadosampler.com/.
(40) Thirugnanasambandam, I.; Vucurevich, T.; Shelton, T.; Kav, N. N. V.; Sheedy, C.; Laroche, A.; Challis, J. K. Assessment of Real-Time PCR Techniques for the Detection of Airborne Fungal Pathogens of Wheat: Role of DNA Extraction on Spore Quantification. *ACS Agric. Sci. Technol.* **2024**, *4*, 1063.
(41) Tang, Z.; Wang, M.; Schirrmann, M.; Dammer, K.-H.; Li, X.; Brueggeman, R.; Sankaran, S.; Carter, A. H.; Pumphrey, M. O.; Hu, Y.; Chen, X.; Zhang, Z. Affordable High Throughput Field Detection of Wheat Stripe Rust Using Deep Learning with Semi-Automated Image Labeling. *Comput. Electron. Agric.* **2023**, *207*, 107709.
(42) Pan, Q.; Gao, M.; Wu, P.; Yan, J.; Li, S. A Deep-Learning-Based Approach for Wheat Yellow Rust Disease Recognition from Unmanned Aerial Vehicle Images. *Sensors* **2021**, *21* (19), 6540.
(43) Ruan, C.; Dong, Y.; Huang, W.; Huang, L.; Ye, H.; Ma, H.; Guo, A.; Ren, Y. Prediction of Wheat Stripe Rust Occurrence with Time Series Sentinel-2 Images. *Agriculture* **2021**, *11* (11), 1079.
(44) He, J.; Wang, L.; Guo, Y.; Zhang, Y.; Zhang, H.; Xu, S.Wheat Stripe Rust Remote Sensing Monitoring Based on a New Vegetation Index*International Conference On Agri-Photonics And Smart Agricultural Sensing Technologies (ICASAST 2022)*SPIEZhengzhou, China20221234918−26
(45) Ma, H.; Zhang, J.; Huang, W.; Ruan, C.; Chen, D.; Zhang, H.; Zhou, X.; Gui, Z. Monitoring Yellow Rust Progression during Spring Critical Wheat Growth Periods Using Multi-Temporal Sentinel-2 Imagery. *Pest Manag. Sci.* **2024**, *80*, 6082.
(46) Hassan, A.; Mumtaz, R.; Mahmood, Z.; Fayyaz, M.; Naeem, M. K. Wheat Leaf Localization and Segmentation for Yellow Rust Disease Detection in Complex Natural Backgrounds. *Alex. Eng. J.* **2024**, *107*, 786−798.
(47) Shafi, U.; Mumtaz, R.; Qureshi, M. D. M.; Mahmood, Z.; Tanveer, S. K.; Haq, I. U.; Zaidi, S. M. H. Embedded AI for Wheat Yellow Rust Infection Type Classification. *IEEE Access* **2023**, *11*, 23726−23738.
(48) Mandava, M.; Vinta, S.; Ghosh, H.; Rahat, I. Identification and Categorization of Yellow Rust Infection in Wheat through Deep Learning Techniques. *EAI Endorsed Trans. Internet Things* **2023**, *10*, 10.
(49) Chen, X. Stripe Rust Epidemiology. In *Stripe Rust*. Chen, X.; Kang, Z.; Springer, Dordrecht: Netherlands, 2017; pp. 283−352. .
(50) Hassan, M. H.; Omar, A. M.; Daskalakis, E.; Mohamed, A. A.; Boyd, L. A.; Blanford, C.; Grieve, B.; Bartolo, P. J. Multi-Layer Biosensor for Pre-Symptomatic Detection of Puccinia Strifformis, the Causal Agent of Yellow Rust. *Biosensors* **2022**, *12* (10), 829.
(51) Blackall, J. L.; Wang, J.; Nabawy, M. R. A.; Quinn, M. K.; Grieve, B. D. Development of a Passive Spore Sampler for Capture Enhancement of Airborne Crop Pathogens. *Fluids* **2020**, *5* (2), 97.
(52) Pollen Sense, L. L. C.*PollenSense. Automated Sensors For Pollen, Mold, Dust Counts*; accessed 2024−10−24, https://www.pollensense.com/.
(53) Davidenko, N.; Schuster, C. F.; Bax, D. V.; Farndale, R. W.; Hamaia, S.; Best, S. M.; Cameron, R. E. Evaluation of Cell Binding to Collagen and Gelatin: A Study of Theeffect of 2D and 3D Architecture and Surface Chemistry. *J. Mater. Sci. Mater. Med.* **2016**, *27* (10), 148.
(54) Long, F.; Peng, H.; Ding, C. Feature Selection Based on Mutual Information: Criteria of Max-Dependency, Max-Relevance, and Min-Redundancy. *IEEE Trans. Pattern Anal. Mach. Intell.* **2005**, *27* (8), 1226−1238.